Appel, F.; Herrmann, D.; Fischer, F.D.; Svoboda, J.; Kozeschnik, E.:
Role of Vacancies in Work Hardening and Fatigue of TiAl alloys
In: International Journal of Plasticity (2012) Elsevier

DOI: 10.1016/j.ijplas.2012.10.001

Role of Vacancies in Work Hardening and Fatigue of TiAl alloys

by

F. Appel[(a)*], D. Herrmann[(a, b)], F.D. Fischer[(c)], J. Svoboda[(d)], E. Kozeschnik[(e)]

[a]Institute of Materials Research, Helmholtz-Zentrum Geesthacht, D-21502 Geesthacht, Germany

[b]now at Wieland-Werke AG, Graf-Arco-Strasse, D-89070 Ulm, Germany

[c]Institute of Mechanics, Montanuniversität Leoben, Franz-Josef-Strasse 18, A-8700 Leoben, Austria

[d]Institute of Physics of Materials, Academy of Sciences of the Czech Republic, Zizkova 22, CZ-616 62 Brno, Czech Republic

[e]Institute of Materials Science and Technology, Vienna University of Technology, Favoritenstrasse 9-11/E308, A-1040 Vienna, Austria

Abstract

The role of vacancies in work hardening and fatigue of TiAl alloys was investigated by mechanical testing and TEM examination of deformed samples. The evolution of the dislocation glide resistance during straining and after recovery was analyzed in terms of thermodynamic glide parameters. Strain path change tests with respect to temperature and recovery experiments were performed in order to characterize the thermal stability of the produced defect structures. The recovery of the deformation induced defect structure was observed by TEM in situ heating experiments. The recovery kinetics is described on the basis of a recently published simulation study of vacancy annihilation.

Keywords: Titanium alumindes, Strain hardening, Fatigue, Vacancies, Debris, Static and dynamic Recovery.

1. Introduction

While there is a voluminous body of literature concerning the structure/property relationships of TiAl alloys, there have been relatively few studies on the factors governing strain hardening. This is in part due to the low tensile elongation, which at room temperature is

*) corresponding author: fritz.appel@hzg.de

usually limited to $\varepsilon = 1$ to 2 %, depending on alloy composition and microstructure. However, in compression it is possible to produce strong work hardening over large plastic strains; the hardening rate being several times greater than that of a typical cubic metal. Gray and Pollock (2002) have assessed the work hardening of intermetallic alloys; Kocks and Mecking (2003) have reviewed the present position with regard to work hardening models in conventional metals. Several aspects of work hardening under monotonic loading might also be important for the fatigue performance of the material. Indeed, depending on the test conditions, a TiAl specimen may cyclically harden, cyclically soften or maintain its flow stress (Hénaff and Gloanec, 2005; Heckel and Christ, 2010; Appel et al., 2010; El-Chaikh et al., 2011).

While these hardening effects are often associated with the evolution of the gross dislocation structure, an often overlooked aspect is that both monotonic and cyclic hardening produces a very high density of fine dislocation debris, with defect dimensions down to the atomic scale. These characteristics of deformation-induced defects could give rise to a strain hardening mechanism with a particular recovery behaviour. This imbalanced view is addressed in the present paper in that strain-induced hardening under monotonic and cyclic deformation is investigated. Particular emphasis is paid on dynamic and static the recovery of the debris structure. These effects are related to the particular point defect situation of TiAl alloys.

2. Experimental investigations

2.1. Deformation experiments

The alloys investigated are briefly characterized in Table 1. The alloys were subjected to a final homogenization annealing at 1030 °C for two hours followed by slow furnace cooling, in order to ensure that the microstructure was sufficiently stable against further recovery annealing at lower temperatures. The work hardening behaviour was investigated under compression in a servo-hydraulic closed loop machine utilizing the sample elongation as feed back parameter. In view of the high yield stress, and in order to avoid elastic buckling, the compression tests were performed on relatively squat samples of 8 mm length and 4 mm diameter. The tests were performed in the temperature range 77 K to 873 K. Deformation at 77 K was carried out in a liquid nitrogen bath. More details for the compression experiments were described in Appel et al. (1997).

The strain dependent flow stress $\sigma(\varepsilon)$ is described as (Schöck, 1965; Kocks et al., 1975; Appel and Wagner, 1998)

$$\sigma(\varepsilon) = \sigma_0 + \sigma_\mu(\varepsilon) + \sigma_D^*(\varepsilon) = \sigma_0 + \sigma_\mu(\varepsilon) + \frac{M_T}{V_D(\varepsilon)}(\Delta F_D^* + kT\, ln(\dot{\varepsilon}/\dot{\varepsilon}_0)), \qquad (1)$$

σ_0 represents a stress contribution from dislocation mechanisms operating at the onset of yielding and is considered to be independent of strain ε. Possible mechanisms associated with σ_0 have been discussed by several authors, for a review see Appel and Wagner (1998); in addition to athermal processes, such as Hall-Petch hardening, σ_0 may also involve thermal contributions that are reflected in the total activation volume V_0 measured at the onset of yielding.

$\sigma_\mu(\varepsilon)$ is an athermal stress contribution to work hardening due to dislocation accumulation and the formation of sessile dislocation locks (Hemker et al., 1993; Veyssière and J. Douin, 1995; Yoo and Fu, 1998; Appel and Wagner, 1998).

Another athermal stress contribution may arise from mechanical twinning. Profuse twinning decreases the mean free path for slip, analogous to a Hall-Petch grain size effect (Appel and Wagner, 1998; Marketz et al., 2003; Appel, 2005). $\sigma_D^*(\varepsilon)$ is an effective or thermal stress component due to thermally assisted overcoming of deformation induced short-range glide obstacles; a prime example is the overcoming of dislocation debris by gliding dislocations. The following terms are used to express $\sigma_D^*(\varepsilon)$: The quantity $M_T = 3.06$ is the Taylor factor, $V_D(\varepsilon)$ is the activation volume of the deformation induced thermal process. Thus, the variation of the reciprocal activation volume with ε will serve as a measure for the contribution of thermal glide obstacles to work hardening. The free energy of activation of this thermally activated process is ΔF_D^*. The quantity $\dot{\varepsilon}_0$ in $\ln(\dot{\varepsilon}/\dot{\varepsilon}_0)$ is a constant reference strain rate, involving the Burgers vector, the mobile dislocation density, the attempt frequency of the dislocations, and the slip path of the dislocations after a successful activation (Beyerlein and Tome, 2008). The energy term kT is the classical Boltzmann energy with k being the Boltzmann constant.

The total activation volume V measured after strain hardening was determined by reversible strain rate cycling tests according to

$$V = \frac{M_T kT}{(\Delta\sigma / \Delta \ln \dot{\varepsilon})_T}, \qquad (2)$$

as described in Appel et al. (1997).

The term $\left(\Delta\sigma/\Delta\ln\dot{\varepsilon}\right)_T$ is the reduced stress increment that occurs upon strain rate cycling at constant temperature *T*. The quantity $\Delta\sigma$ is the difference between the flow stresses σ_1 and σ_2 related to the strain rates $\dot{\varepsilon}_1$ and $\dot{\varepsilon}_2$, respectively. $\Delta\ln\dot{\varepsilon}=\ln(\dot{\varepsilon}_2/\dot{\varepsilon}_1)$ is the logarithm of the strain rate ratio.

It is assumed that $1/V_0$ and $1/V_D\left(\varepsilon\right)$ are linearly additive (Kocks et al., 1975) as

$$\frac{1}{V}=\frac{1}{V_0}+\frac{1}{V_D(\varepsilon)}. \qquad (3)$$

2.2. Dynamic recovery and reversibility tests

Strain path change tests were performed on alloy #3 (Table 1) in order to investigate the reversibility of work hardening with respect to temperature. Compression samples were first deformed at 77 K to strain $\varepsilon = 5.5\%$, unloaded and then re-tested at room temperature. Likewise, other samples were first deformed at room temperature and then re-tested at 77 K. The time between the first and second deformation was typically 20 hours. The reversibility tests were performed under displacement control. The true plastic strains were determined from the total machine displacement by subtracting the elastic deformations of the machine and the sample.

2.3. Static recovery

The thermal stability of the deformation-induced defects was assessed on the high Nb containing alloys #1 and #2a. Compression samples of these alloys were deformed at room temperature to strain $\varepsilon = 6.5\%$, subjected to a 50 hour annealing at 750 °C and re-tested at room temperature. The activation volume was measured before and after the annealing by strain rate cycling tests.

2.4. Low-cycle fatigue

In previous studies (Heckel and Christ, 2010; Appel et al., 2010; El-Chaikh et al., 2011), the fatigue performance of the high-strength alloy #2b with composition Ti-45Al-8Nb-0.2C was investigated. Fully reversed isothermal tests were performed under strain control at temperatures of 25 °C, 550 °C and 850 °C and a total (elastic plus plastic) strain amplitude of $\Delta\varepsilon_t/2 = 0.7\%$.

2.5. TEM observations

The defect structures produced by room temperature work hardening and cyclic hardening were examined by conventional and high-resolution transmission electron microscopy (TEM), utilizing the Philips instruments 400 T, CM-200 and CM-30, operated at 120, 200 and 300 kV, respectively. TEM in situ heating experiments were performed on thin foils prepared from fatigued samples in order to directly observe the recovery of the deformation induced defect structures.

3. Results and discussion

3.1. Macroscopic work hardening phenomena

The detailed shape of the stress/strain curve depends on a number of variables such as alloy composition, microstructure and temperature. Fine-grained high Nb containing alloys (such as alloy #1) often show a yield drop or a plateau region at the beginning of deformation followed by fairly linear work hardening (Fig. 1). Between room temperature and 873 K work hardening is relatively insensitive to temperature as indicated by the family of parallel stress/strain curves. Figure 2a shows the normalized work hardening coefficient, $\vartheta/\mu = (1/\mu)d\sigma/d\varepsilon$, as function of strain ε . The temperature dependent values of the shear modulus μ were taken from Schafrik (1977). Under steady state conditions, $\varepsilon = 6\%$ and $\dot{\varepsilon} = 10^{-5} s^{-1}$, the normalized work hardening coefficient is typically $\vartheta/\mu = 0.04$ to 0.08. Interestingly, in spite of their high yield stresses of the high niobium containing alloys, their work hardening coefficients are similar to those of conventional TiAl alloys.

3.2. Jog dragging and debris hardening

Figure 3a demonstrates the typical microstructure that was observed after room temperature deformation. The vast majority of dislocations had the Burgers vector b=1/2<110], which is in accordance with TEM observations made on other two-phase alloys (Vasudevan et al., 1989; Li and Loretto, 1995; Appel and Wagner, 1995; Sriram et al., 1997; Appel and Wagner, 1998;

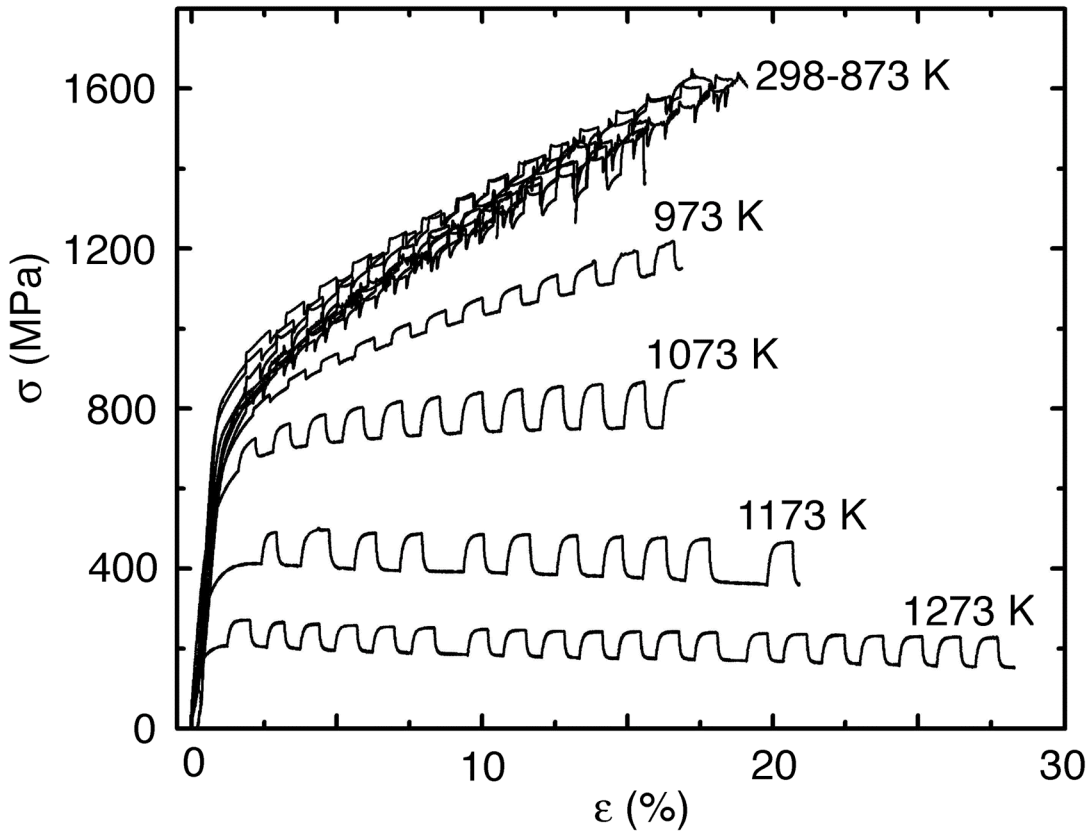

Fig. 1. Load/elongation traces of compression tests demonstrating the work hardening behaviour of nearly lamellar Ti-45Al-8Nb-0.2C (alloy #2a). Reversible strain rate changes were performed between $\dot{\varepsilon} = 2.3x10^{-5} s^{-1}$ s^{-1} and $\dot{\varepsilon}_2 = 20\dot{\varepsilon}_1$; at *T*=1273 K the strain rate ratio was $\dot{\varepsilon}_2 = 3\dot{\varepsilon}_1$.

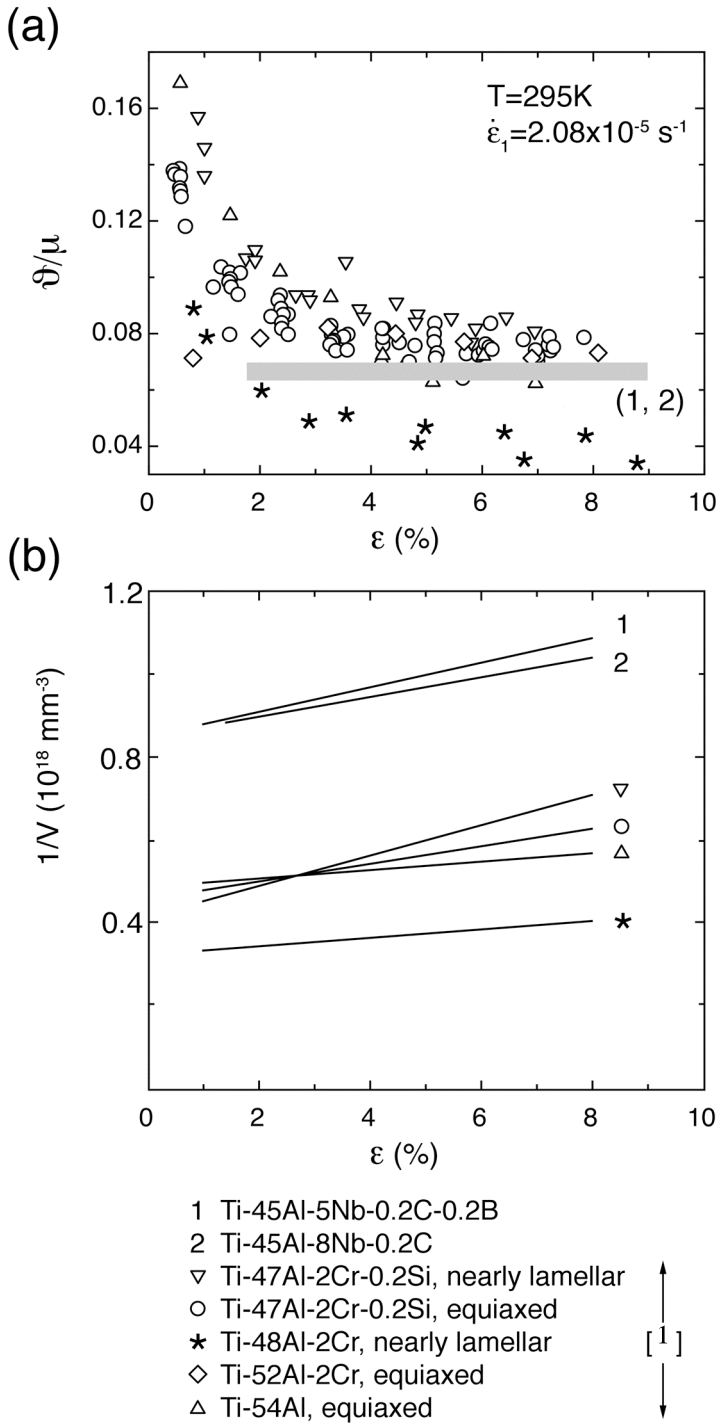

Fig. 2. Work hardening characteristics of TiAl alloys. (a) Dependence of the normalized work hardening coefficient $\vartheta/\mu = (1/\mu)\,d\sigma/d\varepsilon$ and (b) of the reciprocal activation volume $1/V$ on strain ε measured at T=295 K. The shear modulus is μ. Data set [1] from Appel et al. (1999).

Wiezorek et al., 2000; Singh et al., 2006). A characteristic feature is a dense structure of dislocation dipoles (arrows 1) with a size distribution varying from 200 nm down to vanishingly small loops, which are referred to collectively as debris. The defects exhibit inside-outside contrast on reversing $g\{\pm 111\}_\gamma$, indicating their dipolar nature (Thomas and Goringe, 1979). The dipoles are almost perpendicularly elongated with respect to the Burgers vector, i.e., the two dipole arms have edge character and are situated on parallel glide planes. It should be noted that for a given Burgers vector the apparent dipole separation is different for the +g and -g diffraction vectors.

Figure 3b is a high-resolution image of a small debris defect, which under weak beam conditions appeared as a hardly visible dot-like feature. The image was taken along the $<\bar{1}01]$ direction across the two edge dislocation arms of the defect. These unlike dislocations are seen as terminated $(\bar{1}1\bar{1})_\gamma$ planes, each of which corresponds to a projected Burgers vector component $b_p=1/4<\bar{1}2\bar{1}]$ in the $(\bar{1}01)$ plane. This is consistent, for example, with a mixed ordinary $1/2<1\bar{1}0]$ dislocation, a superpartial dislocation $1/2<01\bar{1}]$ and a $1/2<\bar{1}\bar{1}2]$ superdislocation, which all occur in the $L1_0$ structure of γ(TiAl). As indicated by the Burgers circuit, the total Burgers vector of the two dipole dislocations adds up to zero. The (111) plane indicated in the micrograph is continuous and is therefore the slip plane of the two dislocations constituting the dipole. The slip planes are separated by only a few atomic spacings, i.e , the micrograph represents a very narrow dipole with vacancy (extensional) character.

Isolated ordinary dislocations are preferentially aligned along their screw orientation and frequently exhibit cross slip. This, together with the fact that the origin of a dipole is often traceable back to ordinary dislocations (arrow 2 in Fig. 3a), suggests that the debris was trailed and terminated at jogged screw dislocations (collectively called jog dragging). A jog in a screw dislocation has edge character and is unable to move conservatively together with the screw dislocation, (Fig. 4a). At a sufficiently high stress, a screw dislocation may drag a mono-atomic jog along, which will leave behind a trail of vacancies or interstitial atoms depending on the sign of the dislocation and the direction the dislocation is moving. At taller jogs, dislocation dipoles are trailed as the screw dislocation moves, i.e., the jog is connected to the moving dislocation by two lengths of edge dislocations of opposite sign, as sketched in Fig. 4b and exemplified in Fig. 3a (arrow 1). Because of the mutual attraction of the positive and negative edge dislocations forming the dipole, a dipole may break up in a row of prismatic loops. The pinching off of dipoles could be supported by unbalanced sideward

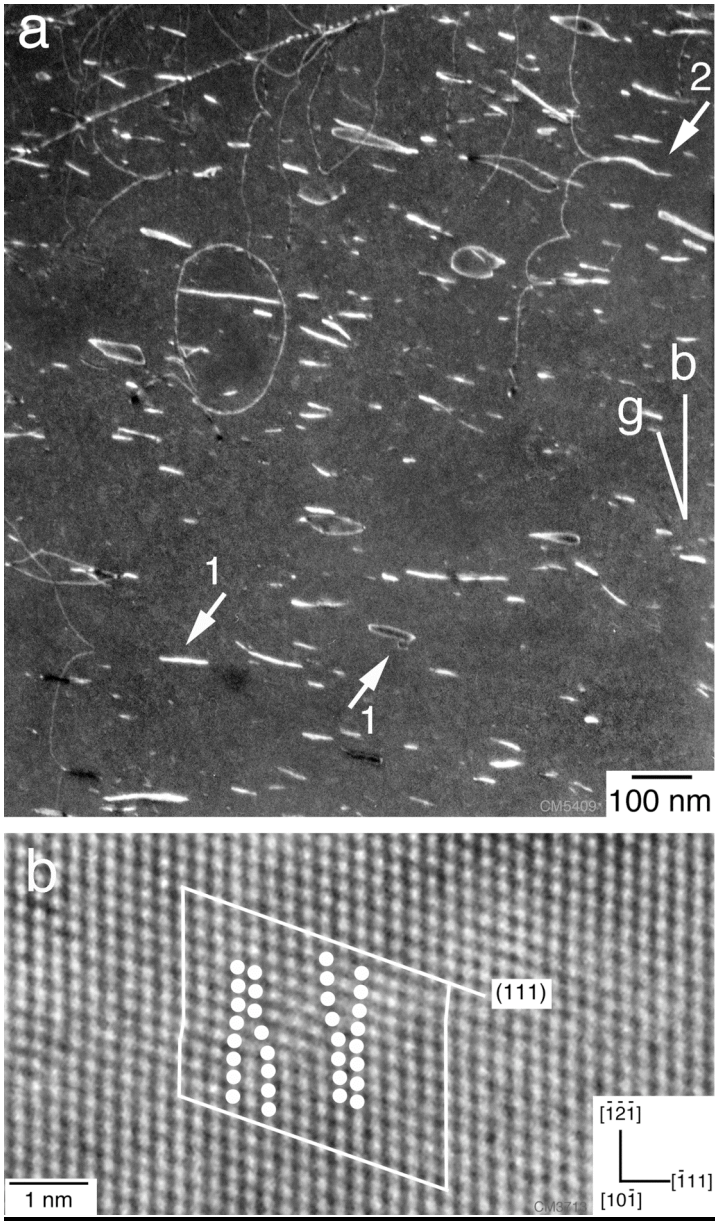

Fig. 3. Dipole and debris structures observed in a nearly lamellar Ti-48Al-2Cr (alloy #3) after room temperature compression to strain $\varepsilon = 3\%$. (a) Pseudo-weak beam image from near the $<\bar{1}01]$ pole utilizing $\{111\}_\gamma$ reflections in the g/3.1g condition. Arrows 1 mark small edge dislocation dipoles showing either inside or outside contrast. The isolated dislocations and the debris defects have the Burgers vector b=1/2<110]. The jogged screw dislocation (arrow 2) is about to trail a dipole. (b) High-resolution image along the $<\bar{1}01]$ direction showing a small dipole across its two edge dislocation arms. The (111) plane indicated is the slip plane of the two dipole dislocations. The unlike edge dislocations are separated by a few atomic spacings indicating the vacancy character of the dipole. The total projected Burgers vector of the dipole configuration is zero, as indicated by the Burgers circuit.

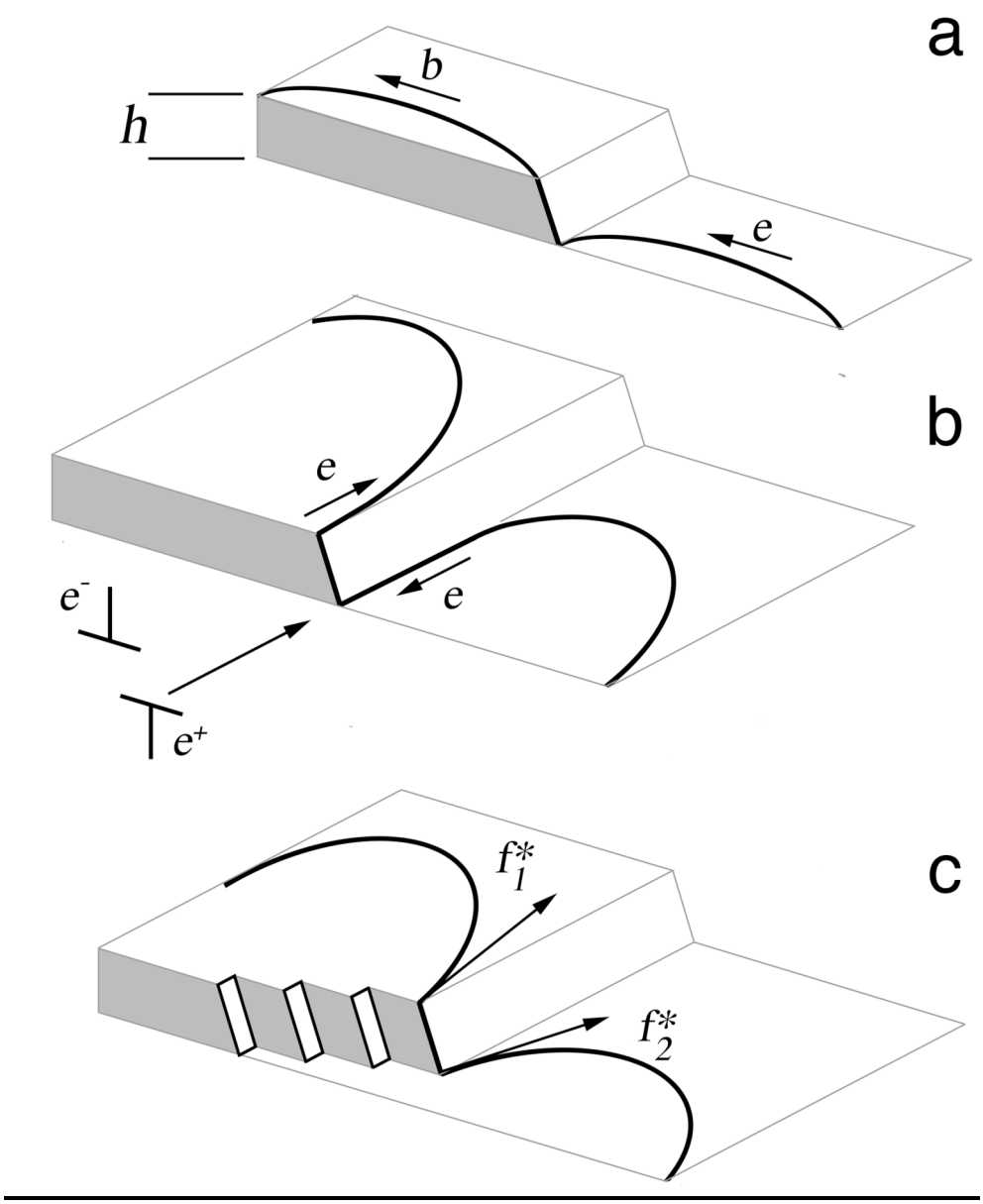

Fig. 4. Schematic illustration of jog dragging processes; *h*-jog height, *b*-Burgers vector of the screw dislocation, *e* dislocation line vector. The cross slip plane for conservative glide of the jog along the screw dislocation is marked light grey. (a) A jog in a right handed screw dislocation. (b) Dipole dragging; the two lengths of edge dislocations of opposite sign form a dipole with vacancy character. (c) Combined lateral glide and forward dragging of the jog due to unbalanced line tension forces f_1^* and f_2^*, resulting in a row of prismatic-loop debris in the wake of the gliding screw dislocation. The orientation of the debris row is slightly inclined to the dislocation line.

forces acting on the jog because these forces give rise to conservative glide of the jog along the dislocation (Fig. 4c). This mechanism may explain why extremely fine debris with a nearly equiaxed morphology is formed (Fig. 3).

In principle, a jogged screw dislocation can acquire both vacancy- and interstitial-producing jogs. However, the stress required for the forward motion of the dislocation producing point defects is proportional to the formation energy of the relevant point defect. Molecular dynamic simulations of Wang et al. (1997) based on Finnis-Sinclair many-body potentials have shown that the formation energies for all the stable interstitial configurations in TiAl are two to three times those of vacancies. Thus, it is unlikely that jog dragging generates interstitial atoms. This consideration may explain why in the present study only vacancy dipoles have been observed (Fig. 3b).

There are several factors that may support cross slip of ordinary dislocations in TiAl. Unlike superdislocations, the ordinary dislocations are not dissociated because the complex superlattice stacking fault (CSF) that would be involved in the dissociation has a very high energy (Yoo and Fu, 1998). Thus, the dislocations need not be constricted before cross slipping, which makes the process easier. For an ordinary dislocation gliding on the primary (111) plane the potential cross slip planes are the $\{110\}_\gamma$, $\{\bar{1}\,\bar{1}\,1\}_\gamma$ and $\{001\}_\gamma$ planes. Sun (1999) and Jiao et al. (2002) have considered the energetic driving forces for cross slip by determining the line tension of an ordinary screw dislocations on these planes. The line tension was found to be lowest for the {110) planes, intermediate for the {111} planes and highest for the (001) planes, a result that is in accordance with TEM observations of Feng and Whang (2000). Thus, an ordinary dislocation gliding on its primary (111) plane is intrinsically prone to cross slip on a $\{\bar{1}10\}_\gamma$ plane or on the oblique $\{\bar{1}\,\bar{1}\,1\}_\gamma$ plane. Thus, the stresses set up by heterogeneities in the deformed state can easily initiate cross slip. Sources of internal stresses are certainly the constraint effects that develop upon loading between the individual constituents of the alloys, as demonstrated by Brockman (2003) utilizing three-dimensional finite-element simulations of the deformation of a nearly lamellar $\alpha_2(Ti_3Al+\gamma(TiAl)$ alloy.

Figure 5 demonstrates a specific example of the effect of local stress concentrations produced by intersecting slip bands. In most, if not all, regions examined after room temperature deformation, double 1/2<110] slip on oblique $\{\bar{1}\,\bar{1}\,1\}_\gamma$ planes was detected. The two sets of intersecting dislocations were separately imaged by appropriate diffraction conditions. The significant feature is the high density of debris that is trailed and terminated in the zone of intersection by each set of dislocations, which could be rationalized by the

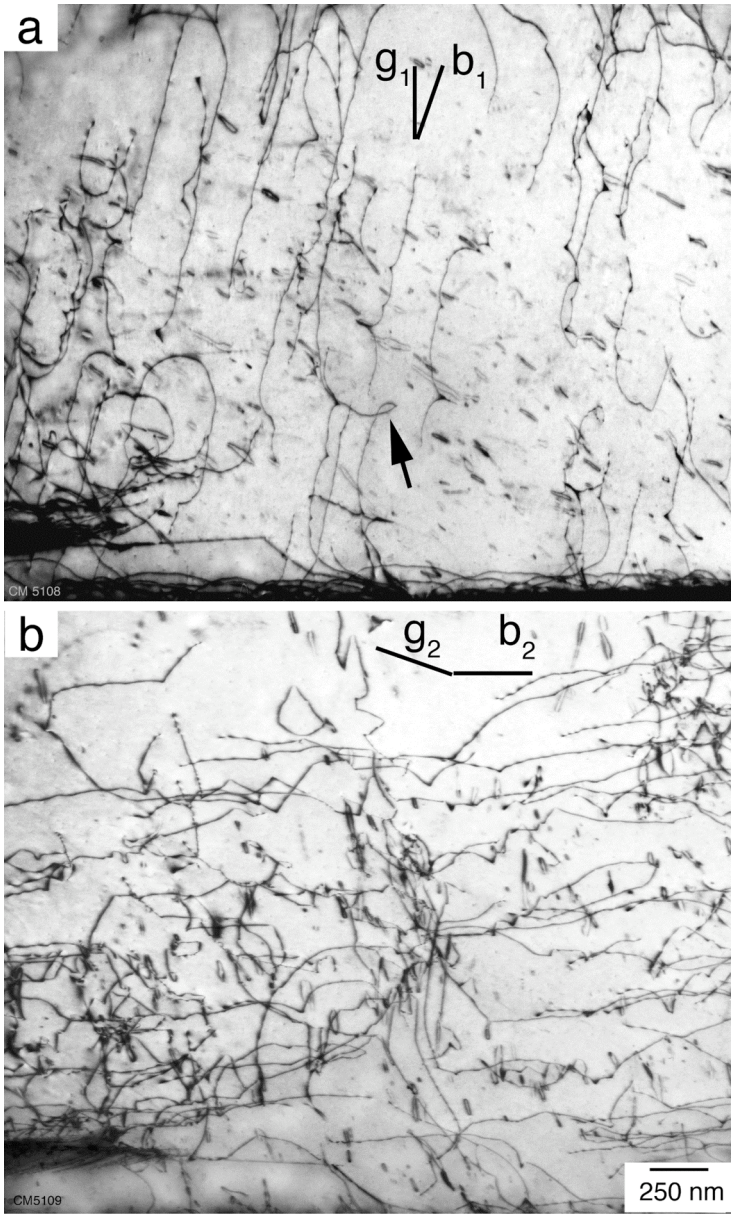

Fig. 5. Intersection of two sets of 1/2<110] dislocations that propagated on oblique {111} planes. Ti-48Al-2Cr, compression at 300 K to strain ε=3%. High-order bright field image from near the $[0\,\bar{1}\,1]$ pole. Note the high density of debris with widely separated dipole arms formed in the intersection zone. (a) Set 1: screw dislocations with Burgers vector b_1=1/2<110] situated on $(\bar{1}\,1\,\bar{1})$ and imaged with g_1=(111). The arrowed detail shows a dipole trailed at a high jog, apparently about to multiply. (b) Set 2: screw dislocations with Burgers vector b_2=1/2<1 $\bar{1}$ 0] situated on $(\bar{1}\,\bar{1}\,1)$ and imaged with g_2=$(1\,\bar{1}\,\bar{1})$.

following arguments. The elastic stresses occurring between the intersecting dislocations are in the order of μ/50 with a significant component acting out of the slip plane (Appel, 1989). The interaction stresses are as high as the yield stress of the material and do not only tend to immobilize the dislocations, but also induce extended cross slip (Appel, 1991). Thus, many jogs formed in the intersecting dislocations are significantly higher than those expected from the simple intersection geometry according to the mutual orientation of their Burgers vectors. This is also indicated by detail 1 in Fig. 5a, which shows a screw dislocation containing a very high jog. Thus, the two dipole dislocation trailed at the jog could overcome their elastic interaction forces and pass each other. Each dipole dislocation then may independently bow out and act as a dislocation source in a fashion similar to a Frank-Read mechanism. This reasoning is in accordance with Fig. 3b, which shows that even the smallest dipoles are significantly higher than those that would be trailed from elementary intersection jogs. It is obvious that this extremely high density of debris within the intersection zone retards further dislocation glide.

In their early papers Gilman (1962) and Chen et al. (1964a, b) proposed that the debris left after deformation may act as additional dislocation glide obstacles. However, investigations of Kroupa (1962, 1966a, 1966b), Bullough and Newman (1970) and Bacon et al. (1970) have shown that the interaction forces between a dislocation and a prismatic dislocation loop are very small and localized. By virtue of these characteristics, the dislocations, with the aid of thermal activation, can probably overcome the debris (Appel and Wagner, 1998; Appel et al., 1999). The related activation volume of this process is described by $V_D = l_D \, \Delta R_D \, b$; l_D is the debris distance and ΔR_D the obstacle diameter. As l_D is expected to decrease with strain, the dragging mechanism should be manifested by an increase of the reciprocal activation volume with strain. As demonstrated in Fig. 2b, this is indeed a salient feature of the room temperature work hardening of TiAl alloys and confirms the model underlying Eq. (1). Essentially the same recovery behaviour was recognized on alloy #2a. The experimental findings coincide with earlier investigations (Appel et al., 1999) that have been performed on TiAl alloys of the second generation with the base-line composition Ti-(47-48)Al. Thus, jog dragging, debris hardening and the easy recovery of the related point defect structures seem to be general work hardening phenomena of TiAl alloys.

3.3. Thermal stability of work hardening

Figure 6 shows a load/elongation trace of a room temperature compression experiment performed on the high Nb containing alloy #1, followed by isothermal annealing

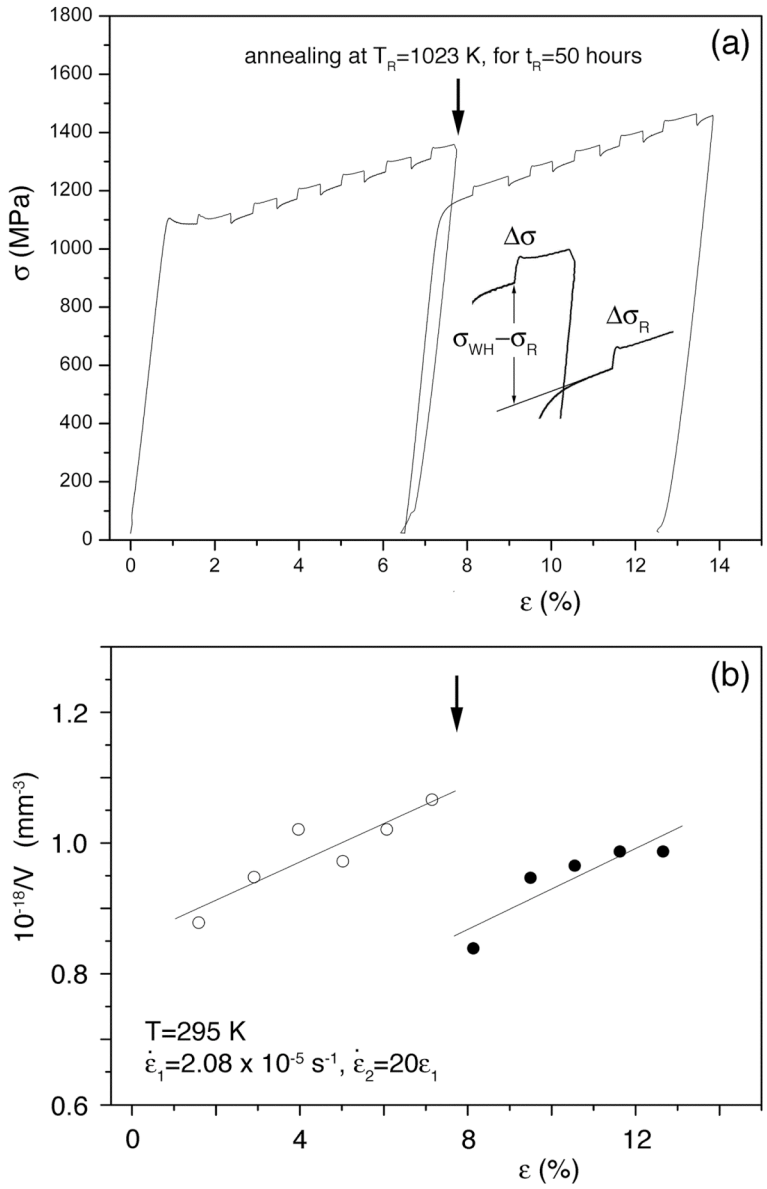

Fig. 6. Recovery of work hardening observed on the extruded Ti-45Al-5Nb-0.2B-0.2C (alloy #1); σ flow stress and V activation volume determined during pre-deformation at 295 K; σ_{WH} flow stress measured after room temperature work hardening, σ_R flow stress measured after annealing. $\Delta\sigma$ and $\Delta\sigma_R$ are the stress increments of strain rate cycling tests for determining the activation volume before and after annealing. (a) Load/elongation trace of a recovery experiment involving pre-deformation in compression at room temperature to strain $\varepsilon_p = 6.5\%$, followed by a 50-hour annealing at 1023 K and subsequently re-tested at room temperature. Reversible strain rate changes were performed for determining the activation volume. (b) Reciprocal activation volume $1/V$ determined in this test before and after the annealing.

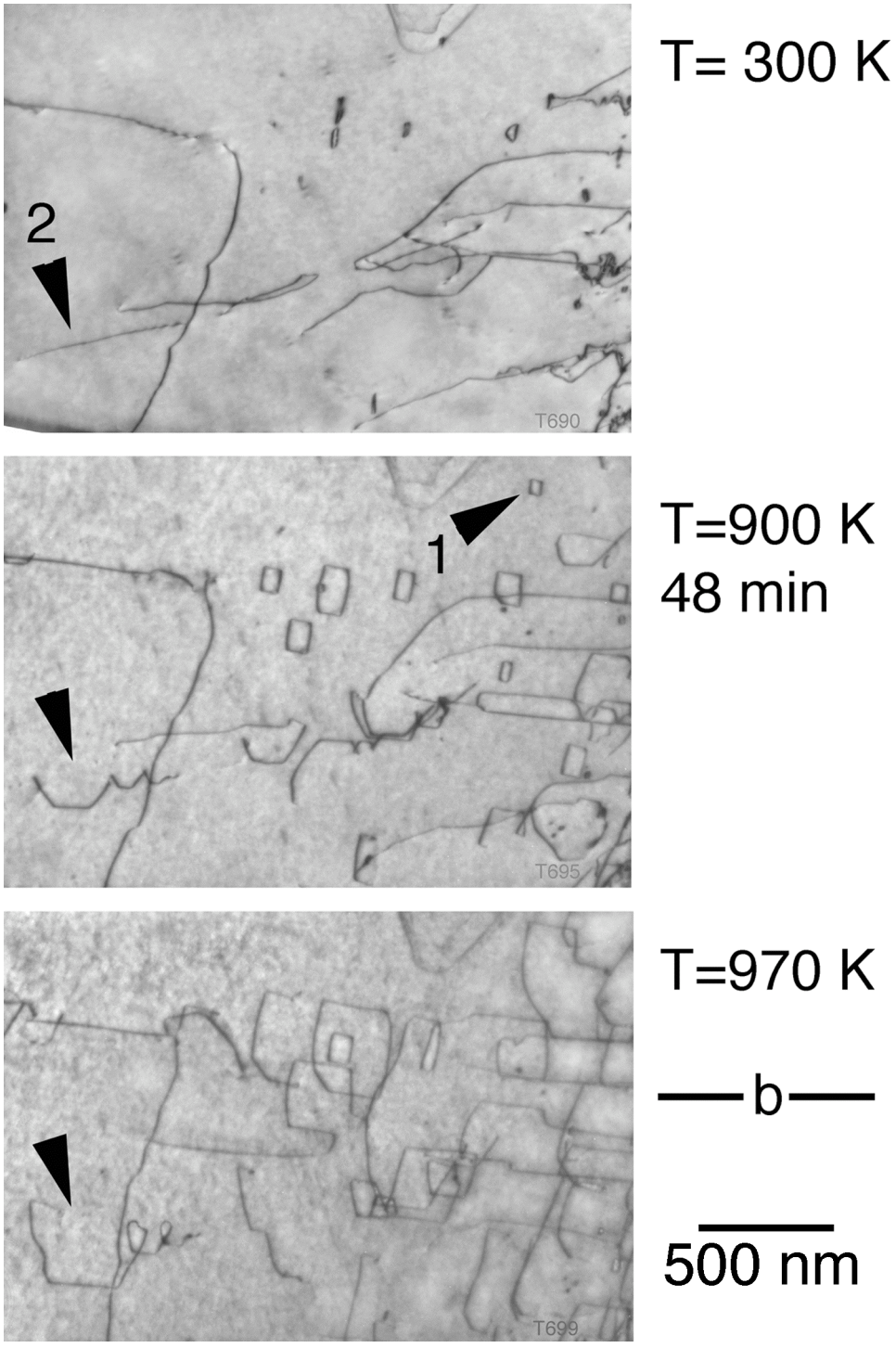

Fig. 7. Defect recovery during in situ heating inside the TEM. Note the growth of the debris defects, the generation of a new loop (arrow 1), presumably due to the aggregation of excess vacancies (arrow 1) and the formation of helical dislocations (arrow 2), because of vacancy absorption. Ti-48Al-2Cr, pre-deformation at room temperature in compression to ε=3%. Acceleration voltage 120 kV.

at 750 °C and re-tested at room temperature. Strain rate cycling tests were performed to determine the activation volume before and after annealing. The two points that most clearly emerge from Fig. 6 are:

(i) A significant amount of the work hardening developed during the initial deformation is lost by annealing;

(ii) recovery of the flow stress is accompanied by a nearly complete recovery of the reciprocal activation volume to the value measured at the beginning of the pre-deformation.

Figure 7 shows a TEM in situ study that may illustrate the defect processes associated with these recovery characteristics. The thin foil was prepared from a sample compressed at room temperature, which produced a dense point defect and debris structure. The micrographs show debris defects growing upon heating, presumably by absorption of excess vacancies. In virtually defect free zones new loops appear, as indicated by arrow 1. This suggests that the excess vacancies condense into disc shape configurations, which collapse to form a dislocation loops. The vacancies seem also to condense onto screw dislocations, causing them to climb into helices (arrow 2). Due to these processes an interconnected and tangled loop structure is formed. Likewise, dislocations of opposite Burgers vectors constituting the tangled loop structure can easily be annihilated by a combination of glide and climb.
The essential point is, however, that the debris defects lose the character of short-range obstacles, which is fully consistent with the observed recovery of the reciprocal activation volume.
Importantly, significant recovery of the flow stress occurs already at 673 K after a very short annealing time of 15 min (Appel et al., 1999). This observation is surprising as the annealing temperature is only $0.38T_m$, a temperature at which conventional bulk diffusion is still ineffective (Mishin and Herzig, 2000). There are mainly three factors that may support low-temperature recovery.

First, the vacancy supersaturation produces a significant chemical potential or a thermodynamic force, which drives the vacancy flux towards sinks until the equilibrium vacancy concentration is achieved.

Second, it might be expected that pipe diffusion along dislocation cores occurs; the energy for this process is about half that for bulk diffusion (Hirth and Lothe, 1992). Based on discrete dislocation dynamics simulations, Gao et al. (2011) have incorporated pipe diffusion into a novel dislocation climb model.

Third, it also appears possible that diffusion in Ti-rich alloys is supported by the presence of a significant anti-structural disorder. The off-stoichiometric deviations of these alloys, of course, are largely accommodated by the formation of α_2 phase according to the phase diagram. However, the $\alpha/\alpha_2 \rightarrow \gamma$ phase transformation involved in the phase separation is sluggish and often cannot be established within the constraints of processing routes. Thus, a significant portion of the excess Ti is taken up by the γ phase. There is good evidence that no structural vacancies are formed in γ(TiAl) (Yoo and Fu, 1998). Hence, in γ(TiAl) the excess Ti is accommodated by the formation of substitutional antisite atoms. These are Ti atoms situated on the Al sublattice (designated as Ti_{Al}). Ti_{Al} antisite atoms associated with vacancies (called antistructural bridges) may significantly support low temperature diffusion, where conventional vacancy driven diffusion is still ineffective (Mishin and Herzig, 2000). These antistructural bridges allow sublattice and inter-sublattice jumps of the vacancies, without disturbing the long-range order of the γ-phase. Using molecular dynamic calculations, Mishin and Herzig (2000) have shown that the activation energy for an antistructural bridge mechanism involving Ti_{Al} antisite defects is significantly lower than the migration energy of thermal vacancies.

However, long-range diffusion via antistructural bridges is only possible if the concentration of antisite defects exceeds a certain critical value, the so-called percolation threshold. Below this critical value, the sub-structure of the antistructural bridges is not continuous, and diffusion is confined to isolated clusters. Unfortunately, the percolation threshold concentration of Ti_{Al} antisite defects are not known for TiAl. In the alloys investigated the Ti concentration of the γ phase increases when the alloy becomes richer in Ti until the maximum solubility of Ti in the γ phase is reached. At the eutectoid point of the binary Ti-Al system the solubility of excess Ti is about 3 at. %, and so is the concentration of Ti_{Al} antisite defects (Fröbel and Appel, 2002). Although this Ti_{Al} concentration is very high, the question remains, whether it is above the percolation threshold or not.
Whereas the increase of the reciprocal activation volume completely recovers at these low temperatures and short annealing times, the flow stress increase obtained by work hardening

is not completely recoverable. This indicates that long-range obstacles to dislocation motion, such as sessile dislocation locks, have not been removed.

3.4. Dynamic recovery - effect of strain path change

Under steady-state deformation conditions, work hardening and dynamic recovery are competing processes, the balance of which mainly depends on temperature. The question arises under which conditions the deformation structure may recover dynamically? In this context the reversibility tests described in Sect. 2.2 will be discussed. Deformation at 77 K may be considered as a reference state because dynamic recovery is unlikely at this low temperature. Thus, the stress/strain curve measured at 77 K should solely reflect work hardening.

The data obtained on a variety of alloys shows that the flow stress and work hardening rates at 77 K are significantly higher than those determined at room temperature. As an example, Fig. 8 demonstrates the behaviour observed on alloy #3, which is typical for all the alloys investigated. The increase of the yield stress with decreasing temperature is readily understandable; a lower temperature reduces the probability of thermal activation, which, according to Eq. 1, gives rise to a higher thermal stress component (Eq.1). The point to note is that the higher work hardening rate at 77 K is always associated with a stronger increase of $1/V$ with ε, when compared with room temperature deformation. This indicates a higher accumulation rate of thermal defects at 77 K. The lower deformation temperature could enhance the frequency and extent of cross slip events, which in turn enhances the point defect and debris production. However, there is a remarkable dependence of the work hardening rate on the strain path (Fig. 9). The work hardening rate produced during the primary low-temperature deformation and the related value of $1/V$ are instantly recovered when deformation is continued at room temperature (secondary deformation). The high density of accumulated defects combined with high internal stresses may cause this unusual fast recovery of the low-temperature work hardening. During the subsequent room temperature deformation the defects seem to recombine or to agglomerate so that they are less efficient in hardening the material. Furthermore, dislocations generated during the room temperature deformation may act as sinks or recombination centres for point defects, thereby removing the extra defects produced at the lower temperature. Thus, part of the defects responsible for the primary low-temperature strain hardening is dynamically recoverable at the secondary room temperature deformation, i.e., the secondary stress/strain curve actually reflects a balance between strain hardening and dynamic recovery. As a result, the work hardening rate at the

secondary room temperature deformation is reduced by about 10%, when compared with tests that were solely performed at 295 K. An analogous behaviour was observed for the reversibility test with the primary deformation at 295 K and the secondary deformation at 77 K (Fig. 10). In this case the work hardening rate at 77 K was only 70% of that measured in

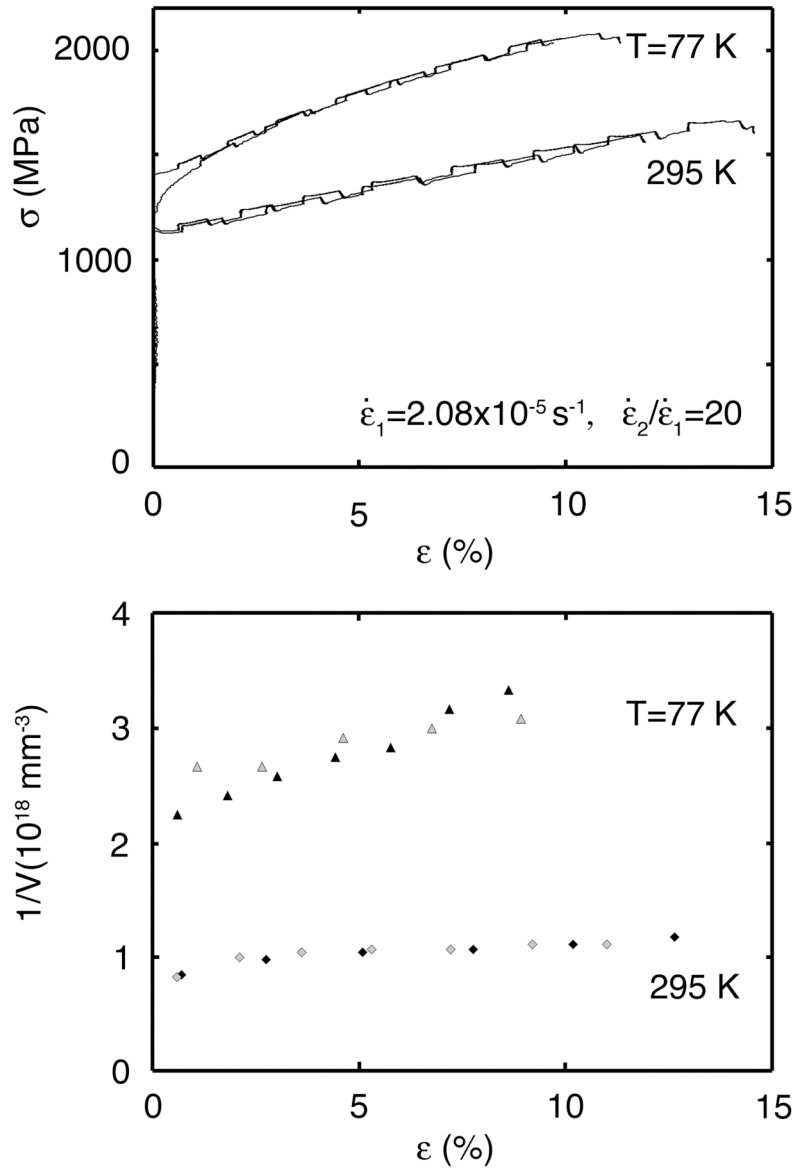

Fig. 8. Deformation behaviour at T = 295 and 77 K. Ti-45Al-10Nb (alloy #3) deformation under displacement control. (a) Two deformation curves at the respective temperatures; (b) variation of the related reciprocal activation volumes with strain.

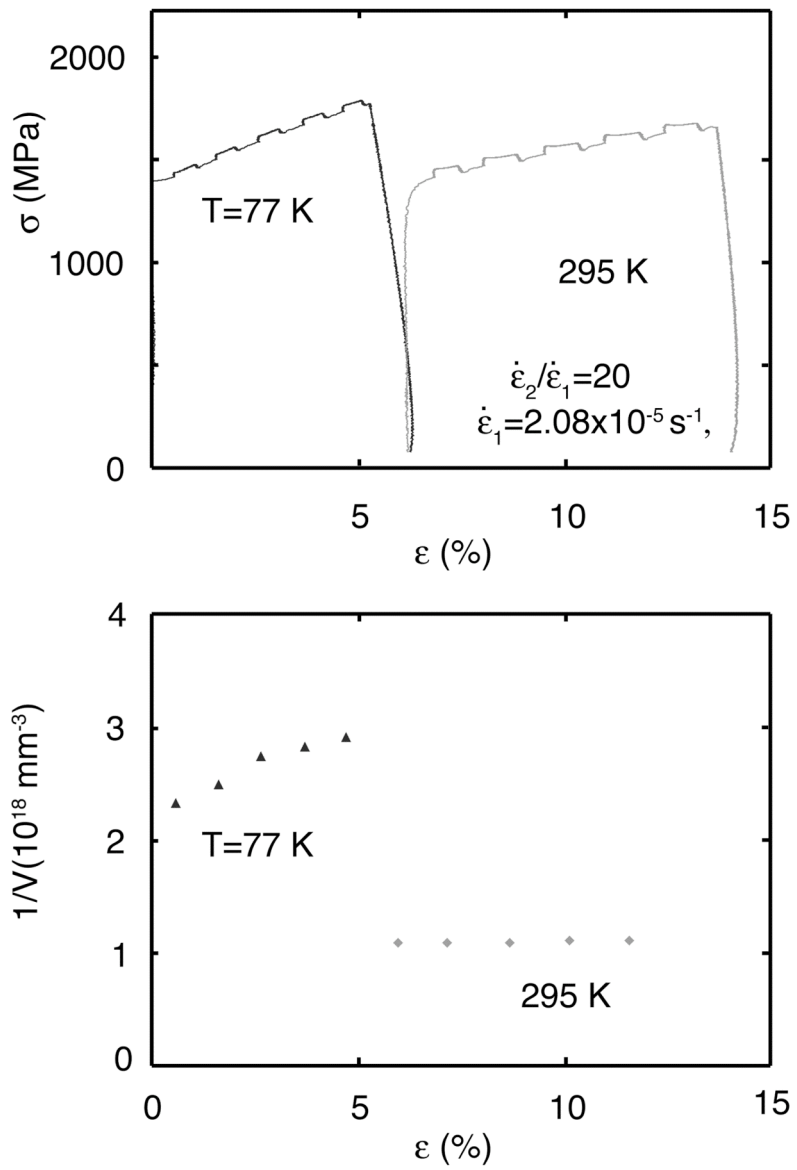

Fig. 9. Dependence of the work hardening behaviour on the strain path. Primary deformation at $T = 77$ K, secondary deformation at 295K. Alloy # 3. (a) Stress/strain curves; (b) variation of the related reciprocal activation volume with strain ε .

tests solely performed at 77 K. Taken together, these factors make the work hardening rates between 77 K and 295 K dependent on the strain history.

Dynamic recovery is usually a phenomenon occurring during high-temperature deformation because the restoration of the defective crystal structure requires diffusion. However, in dynamic recovery, the applied stress producing the deformation is superimposed to the interaction stresses between the various defects. This is unlike to the situation in static recovery, where only the interaction stresses between the dislocations themselves are present. Thus, dynamic recovery can occur at significantly lower temperatures than static recovery. This phenomenon was already demonstrated in the early investigations of Thornton and Cahn (1961) who have shown that recovery of aluminium is greatly accelerated by an applied stress. Concerning TiAl alloys, the difficulty with this scenario is that at more elevated temperatures the effect of dynamic recovery should become stronger because the mobility of dislocations generally increases with increasing temperature. A higher temperature also facilitates cross slip and climb, both of which are required for the generation of the recovered microstructure. Thus, at higher temperatures, lower work hardening is expected. This is clearly not the case since the work hardening is nearly independent between 298 K and 873 K (Fig. 1). A possible explanation is that defect atmospheres at the dislocations are formed above room temperature, as was demonstrated in Fröbel and Appel (2002). The relevant defect species is a Ti_{Al} antisite defect associated with a vacancy, which is capable of reorienting in the dislocation stress field. The resulting locking of the dislocations may impede defect annihilation. The locking effect of defect atmospheres disappears at about 750 K. Thus, above this temperature intensive dynamic recovery and recrystallization probably develop, which is eventually manifested in work softening (Herrmann and Appel, 2009).

3.5. Recovery kinetics of work hardening

The results described in the previous sections suggest that several recovery mechanisms may operate simultaneously. There is a spectrum of defects, involving isolated vacancies, vacancy clusters and debris, which may recover concurrently. Also, tangled dislocations may transform into well-defined networks, lowering the overall energy. The analysis is further complicated by the fact that each recovery mode may have its own kinetics. The problems involved in the analysis of recovery kinetics of non-equilibrium point defect structures were considered in a review of Zehetbauer (1994) to which the reader is referred to for background information. However, a common feature of all these processes is most probably the

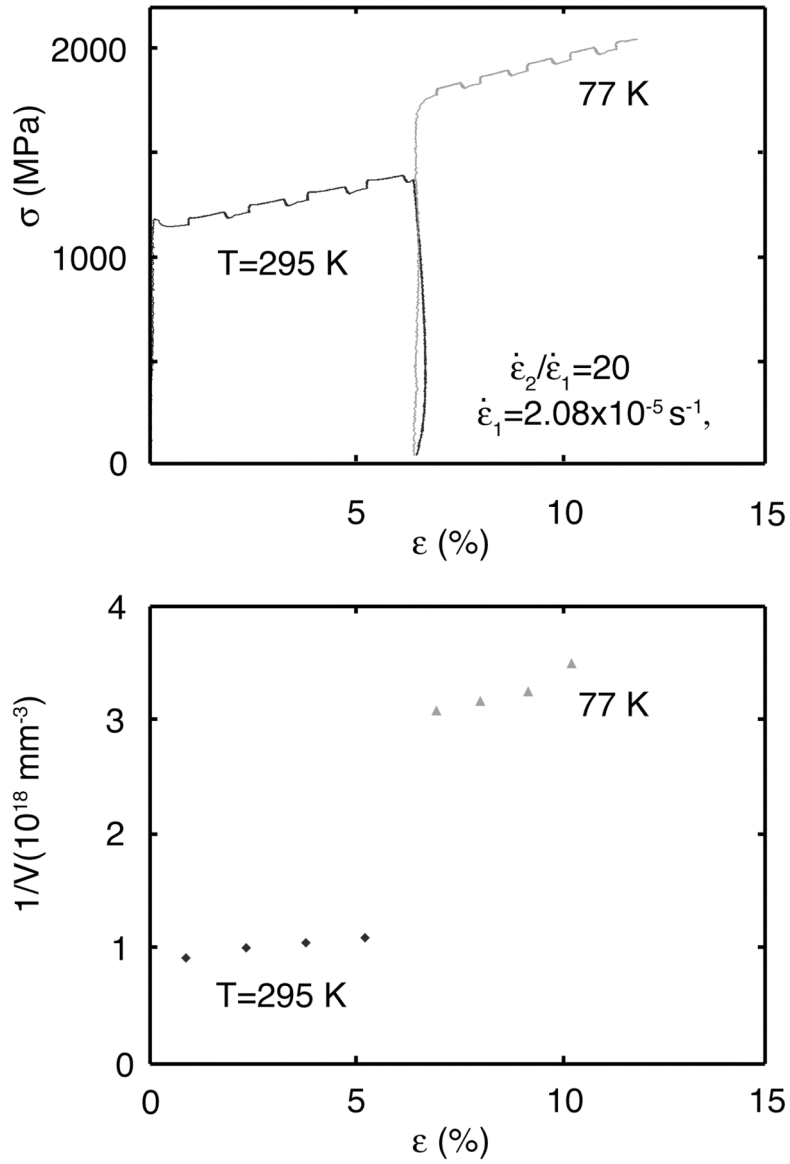

Fig. 10. The same as Fig. 9, but primary deformation at 295K and secondary deformation at 77K. (a) Stress/strain curves; (b) variation of the related reciprocal activation volume with strain ε .

migration of vacancies to sinks where they are annihilated, a problem that was recently addressed by simulation studies (Fischer et al., 2011a, b). The rate process of vacancy annihilation was investigated for different types of sinks as jogs, Frank loops and grain boundaries. In the actual case the debris is considered as line type objects consisting of dipoles of edge dislocations, which may act as sinks for excess vacancies. As shown in Fig. 7, this situation seems to be a characteristic feature of static recovery of deformed TiAl alloys. The debris with the short range stress fields of the dipoles may even trap sliding dislocations and act as "incidental" dislocation boundaries (dislocation walls), see (Hansen and Jensen, 2011). Insofar the distance *d* of these boundaries has reference to the density ρ of debris by a proportionality relation between *d* and $1/\sqrt{\rho}$. The rate of density $\dot{\rho}$ can be assumed to be proportional to the rate $\dot{y}_0$ of the vacancy site fraction y_0 (see discussion concerning Fig. 7). This is the more justified, the more the annihilation rate of vacancies in the debris is spatially constant. This yields the relation $\rho = p\tilde{y}_0 - \left(p\tilde{y}_{0,s} - \rho_s\right)$ with $\tilde{y}_0 = y_0/y_{0,eq}$ and $y_{0,eq}$ being the equilibrium site fraction of vacancies. The quantities $p, \tilde{y}_{0,s}$ and ρ_s are a multiplier and the starting values of $\tilde{y}_0$ and ρ of the annihilation process, respectively. If $\left(p\tilde{y}_{0,s} - \rho_s\right)$ can be neglected in relation to ρ or $p\tilde{y}_{0,s}$, then ρ can be assumed to be proportional to $\tilde{y}_0$ or *d* being proportional to $1/\sqrt{\tilde{y}_0}$.

If we now introduce σ_R as flow stress after recovery and σ_0 as the yield stress without any hardening effect, see also Sect. 2.1, then a Taylor-type argument allows one to assume a direct proportionality of the work hardening contribution $\left(\sigma_R - \sigma_0\right)$ and $\rho^\alpha, 0.2 \le \alpha \le 1$. As an example, the Hall-Petch relation requests $\alpha = 0.25$; for further details see also (Hansen and Jensen, 2011). According to the above discussed proportionality between ρ and $\tilde{y}_0$, we can formulate the following relation for σ_R after replacing of ρ by $\tilde{y}_0$

$$\sigma_R = \sigma_0 + g \cdot (\tilde{y}_0)^\alpha \qquad (4)$$

with *g* being a constant.

For $\tilde{y}_0$ we use Eq. (23.2) in (Fischer et al., 2011a) as general model for the relative vacancy site fraction valid for various vacancy annihilation processes, yielding

$$\tilde{y}_0 = \tilde{y}_{0,s}^{\exp(-\tau)}. \qquad (5)$$

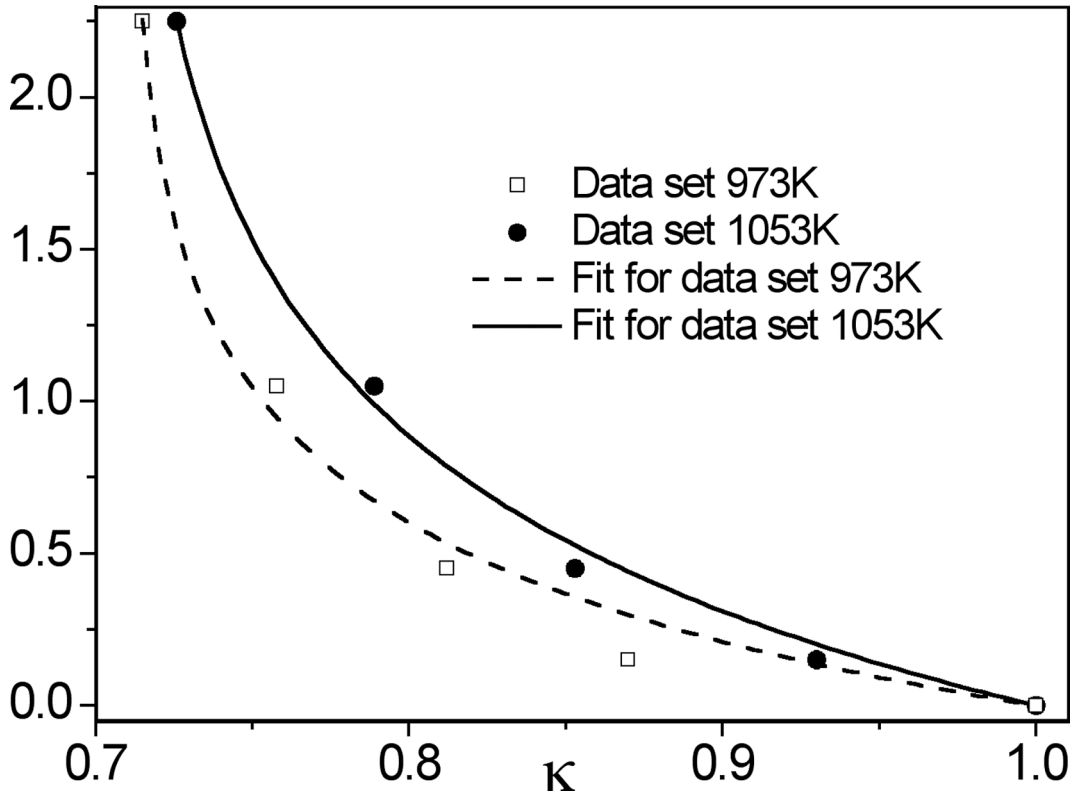

Fig. 11. Evaluation of the kinetics of the recovered flow stress σ_R according to Eq. (9.2), , $t/100=\tilde{t}$ versus κ. Data determined on a forged Ti-47Al-2Cr-0.2 Si alloy with a globular $(\alpha_2+\gamma)$ microstructure (alloy #5), data sets from Appel et al. (1999), Fig. 11 there, for 973K and 1053K; see also Table 2.

A dimensionless time τ is introduced as

$$\tau = tC \tag{6}$$

with the time constant C which reads, e.g. for a time-independent jog density *H*,

$$C = \frac{1}{y_{0,eq}} \frac{\tilde{D}_{eq}}{f} 2\pi a H, \tag{7}$$

for details see sect. 4 of (Fischer et al., 2011a). The quantity $\tilde{D}_{eq}$ represents a temperature dependent diffusion coefficient, *f* a geometrical correlation factor (f=0.7815 for face-centred cubic metals) and *a* the lattice spacing. The time constant *C*, however, will be evaluated below from experimental data and need not be derivated as for the example of jogs. For the further derivation it is also very favourable that the exponent α in Eq. (4) plays no role. Comparing σ_R, Eq. (4) for the state immediately after work hardening (σ_R is replaced by $\sigma_{WH}, \tilde{y}_0$ by $\tilde{y}_{0,s}$), one finds with $\kappa = (\sigma_R - \sigma_0)/(\sigma_{WH} - \sigma_0)$ and Eq. (5)

$$\frac{\ln(\tilde{y}_0)^\alpha}{\ln(\tilde{y}_{0,s})^\alpha} = \frac{\ln\left((\sigma_R - \sigma_0)/g\right)}{\ln\left((\sigma_{WH} - \sigma_0)/g\right)} = 1 + \frac{\ln\kappa}{\ln\left((\sigma_{WH} - \sigma_0)/g\right)} = 1 + \tilde{a}\ln(\kappa) = \exp(-\tau) \tag{8}$$

or finally

$$\ln(1 + \tilde{a} \cdot \ln\kappa) = -\tau\,, \quad \tilde{a} = 1/\ln\left(\sigma_{WH} - \sigma_0/g\right); \tag{9.1}$$

or in slightly modified form with eq. (6)

$$-\tilde{c} \cdot ln(1 + \tilde{a} \cdot ln\kappa) = \tilde{t}\,. \tag{9.2}$$

Eq. (9.1) represents a nonlinear relation between the actual time interval ($\tilde{t} = t/100$) after work hardening and the recovery stress ratio $\kappa = (\sigma_R - \sigma_0)/(\sigma_{WH} - \sigma_0)$. Two parameters are included, namely ã and $\tilde{c} = 1/100C$. Inversion of Eq. (9.1) yields after some analysis

$$\sigma_R = \sigma_0 + (\sigma_{WH} - \sigma_0) \cdot (e)^{[exp(-\tau)-1]/\tilde{a}}, \tag{10}$$

meaning the initial recovery rate is extremely fast.

To make this statement quantitative, Eqs. (9), (10) were used in order to re-evaluate the recovery data that had been previously determined on a Ti-47Al-2Cr-0.2 Si alloy with a globular $(\alpha_2 + \gamma)$ microstructure (Appel et al., 1999). For brevity, the samples were compressed at room temperature to strain $\varepsilon = 7.5\%$ and stress σ_{WH}. Then, the samples were subjected to isothermal annealings and again deformed at room temperature. The flow stress σ_R measured at this secondary deformation was used to monitor the degree of recovery as function of time. For σ_0 the value of 90 MPa is chosen as the lowest value of σ_R in Fig. 11 of (Appel et al., 1999). Figure 11 of this paper demonstrates the relatively good fit of the data, lending support to the model. The experimental data and the fitting parameters are given in Table 2.

3.6. Fatigue structures

Alloy #2b exhibits cyclic hardening at room temperature, almost saturated stress response at 550 °C and cyclic softening at 850 °C. For example, during room temperature cycling, the tensile stress amplitude increased during 641 cycles from 935 to 1050 MPa. Failure typically occurred after N_f=500 to 645 cycles, depending on test temperature (Appel et al., 2010). This observation essentially coincides with the data reported in the literature for different other $\alpha_2\,(\mathrm{Ti_3Al}) + \gamma\,(\mathrm{TiAl})$ alloys (Hénaff and Gloanec, 2005). Samples fatigued at 25 °C and 550 °C exhibited dense structures of debris clusters (Fig. 12a), interspersed by walls of ordinary dislocations (Fig. 12b). As with monotonic deformation (Sect. 3.2), multiple slip is the rule rather than the exception. The debris production seems to be enhanced in neighbourhood of phase boundaries (Fig. 12a), where high constraint stresses are expected to occur, and where under fatigue conditions dislocations are repeatedly immobilized and generated. The high rate of defect accumulation during fatigue may in part result from the fact that the motion of a jogged screw dislocation is not fully reversible. This is because a jog can conservatively glide along a screw dislocation. Thus, on the same dislocation the distribution of the jogs may be different during its to- and fro glide. Then, during its backward motion, the dislocation has to intersect the debris and dipoles previously left in its wake. Furthermore, a

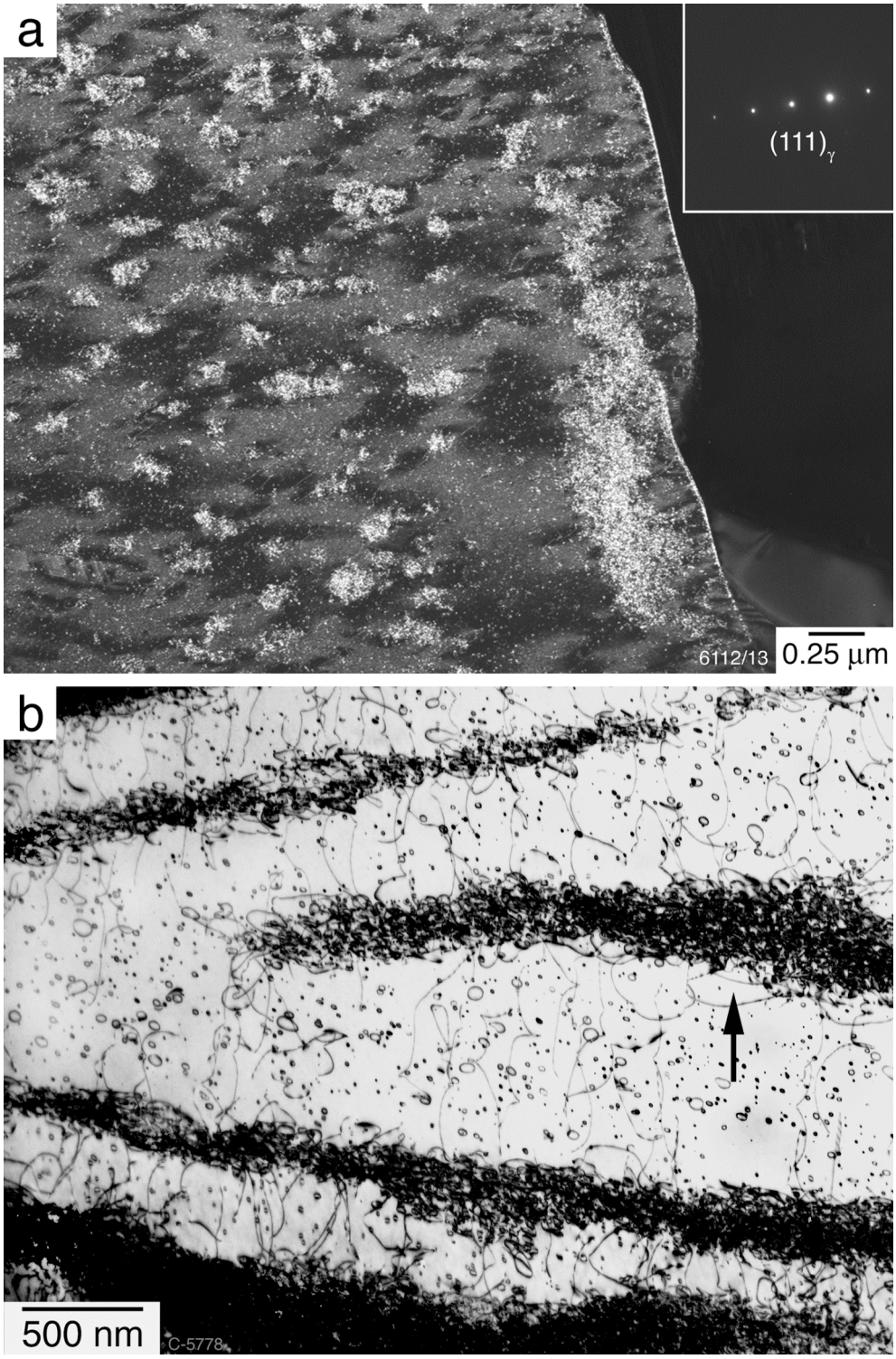

Fig. 12. Deformation structure in Ti-45Al-7.7 Nb-0.2C (alloy #2b) samples fatigued with $R = -1$ and a total strain amplitude of $\Delta\varepsilon_t/2 = \pm 0.7\%$. (a) Debris structure formed after room temperature fatigue to failure after N_f=641 cycles. (b) Dislocation walls (arrowed) and debris observed after fatigue at $T = 550°$ C to failure at N_f=542 cycles.

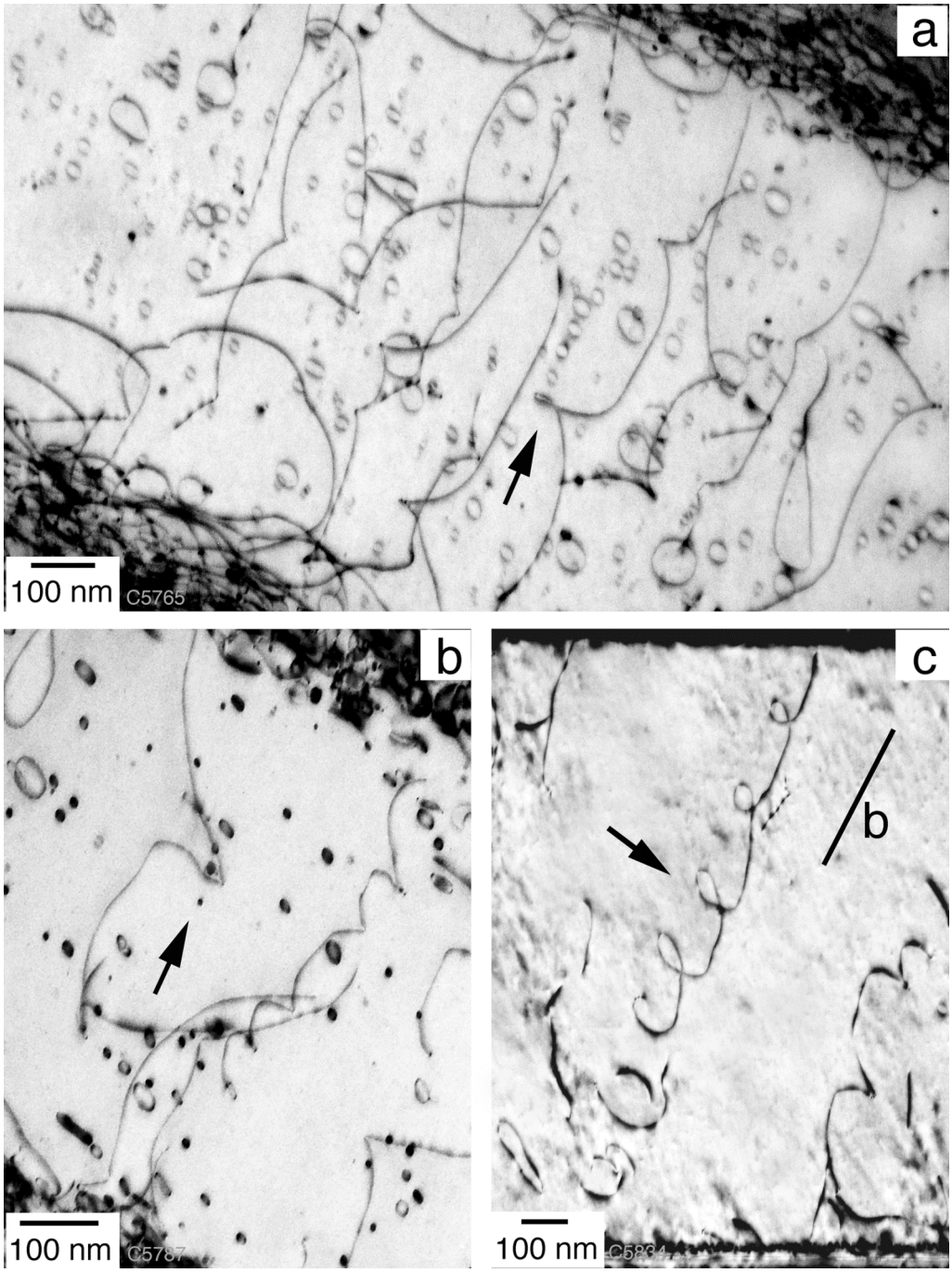

Fig. 13. Debris mechanisms observed in (alloy #2b) after fatigue at $T = 550°$ C to failure at $N_f = 452$ cycles. (a) Dislocation debris trailed and terminated at jogs in ordinary screw dislocations. The debris defects seem to have grown during testing. Note the loop row (arrowed) produced at a high jog, which probably propagated along the dislocation due to unbalanced sideward forces, as schematically sketched in Fig. 4c. (b) Dislocation interactions with debris. Note the anchoring of a dislocation by a cluster of debris defects (arrowed). (c) A helical dislocation (arrowed) probably formed by vacancy condensation onto the dislocation.

vacancy-producing jog has to produce interstitials if it moves in the opposite direction. These factors may cause further cross slip and debris production to occur.

The dislocation walls consist of edge dislocations and dipoles all having the same Burgers vector. The walls are probably formed by the mutual trapping of dislocations due to their elastic interaction. Also, despite their short-range stress fields, dipoles might be able to trap other parallel edge dislocations to form the observed walls (Chen et al., 1964a, b). Due to these processes, the dislocation density can be extremely high in the walls. When compared with room-temperature fatigue, the tendency to form dislocation walls is significantly enhanced at 550°C.

3.7 Recovery of fatigue structures

As with monotonic deformation a remarkable thermal instability of the debris structure has been recognized. This becomes already evident by the defect structure observed after fatigue at 550 °C; Fig. 13 shows the relevant details. Although the debris structure was quite similar to that observed after room temperature fatigue, there are characteristic differences. Whereas clusters of very small debris were predominant in the sample tested at room temperature (Fig. 12a), larger loops and elongated dipoles occurred in the 550 °C sample (Fig. 13a). The debris defects seem to have grown during testing. Rows of prismatic loops, aligned nearly parallel to the average dislocation orientation, is a characteristic feature of the micrograph. These defect rows were probably produced by the combination of conservative lateral glide and forward dragging of the jog and were left in the wake of the dislocation, as described in Sect. 3.2 and illustrated in Fig. 4c. The frequent occurrence of such debris rows indicates that conservative jog propagation on the cross slip plane is relatively easy, i.e., there is no significant additional lattice friction present, when compared with the primary slip plane. This gives rise to the speculation that the cross slip plane is an obliquely oriented $\{111\}_\gamma$ plane rather than the $\{110)_\gamma$ or $\{001)_\gamma$ planes, which are less densely packed.

As with monotonic deformation, arrays of debris seem to retard dislocation motion (Fig. 13b). Most importantly, dislocation helices were observed (Fig. 13c). These findings indicate the onset of dynamic recovery, which for the relatively low test temperature is astonishing but could be rationalized by the arguments given in Sect. 3.3. The other distinct feature of dynamic recovery, the formation of well-defined sub-boundaries, was not observed. However, the dislocation walls frequently occurring at 550 °C could act as a precursor for this process.

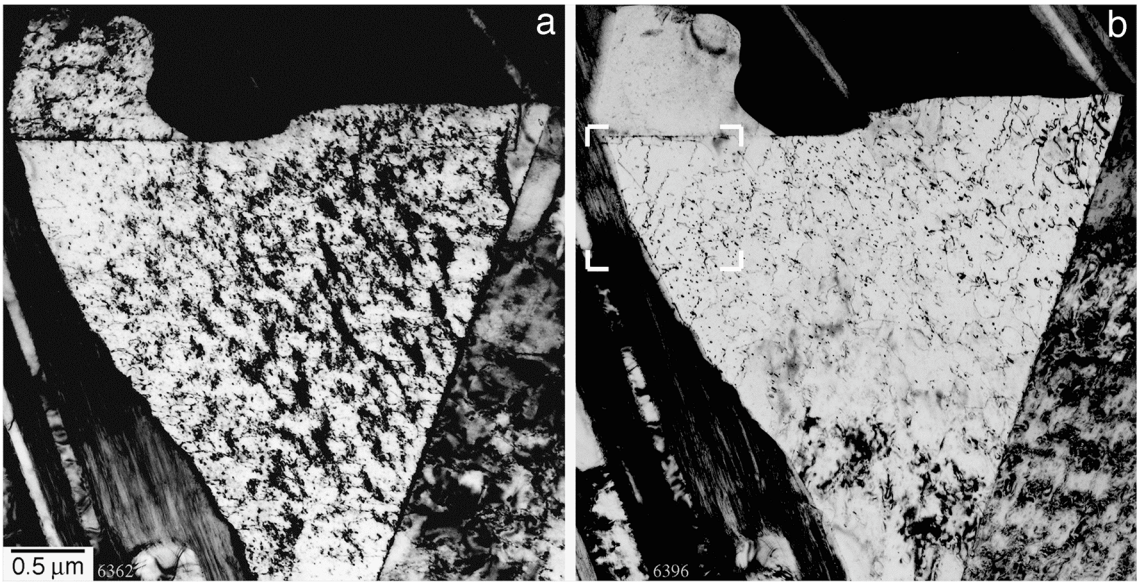

Fig. 14. Recovery of the fatigue structure observed during in situ heating inside the TEM, (alloy #2b). (a) Debris structure of the sample fatigued at room temperature to failure after $N_f = 641$ cycles with a stress ratio $R = -1$ and a total strain amplitude $\Delta\varepsilon_t/2 = \pm 0.7\%$. (b) Recovered structure after annealing at 570 °C for 45 min.

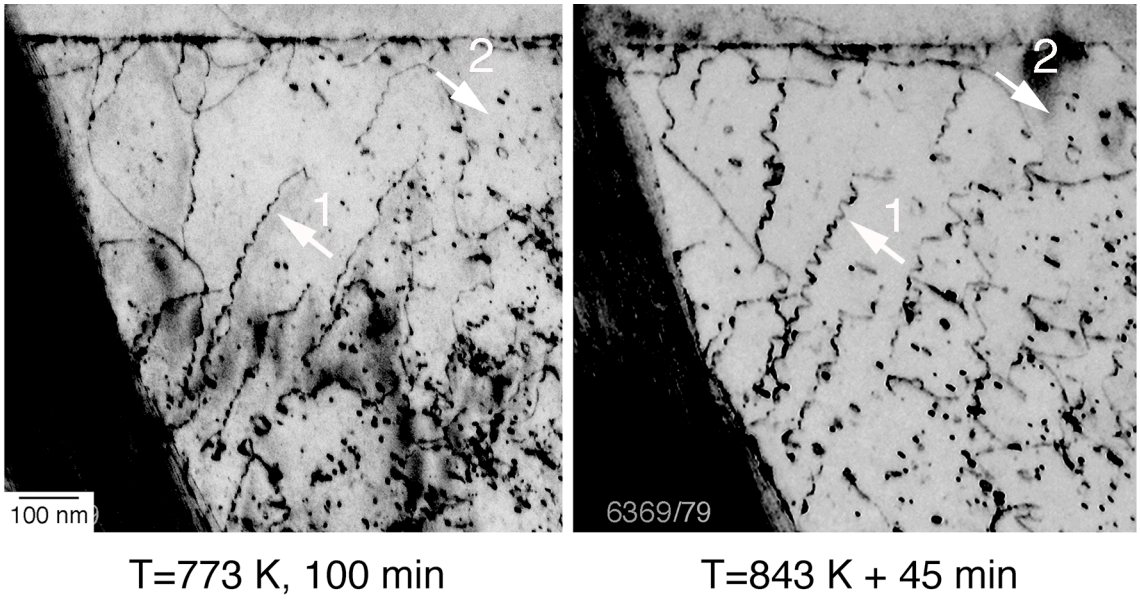

Fig. 15. Dislocation/point defect interactions observed during in situ heating. Higher magnification of the boxed area in Fig. 14 at two intermediate stages of recovery defined in the legend. Note the formation of a spiralled dislocation (arrow 1) and the increased loop size (arrow 2) in the later stage of recovery.

The most convincing evidence of the thermal instability of the fatigue structure was obtained by TEM in situ heating experiments. The thin foils investigated in this study were prepared from specimens fatigued at room temperature and annealed inside the TEM. As demonstrated in Fig. 14, the fatigue structure significantly recovers at moderately high temperatures. Again helices are formed (Fig. 13c), giving further evidence to believe that dislocation climb has taken place. During the thermal cycle illustrated in Figs. 14 and 15, dislocation annihilation and rearrangement into stable configurations occur. Thus, recovery of fatigue structures seems to be more complex. Nevertheless, the observations may explain why in samples fatigued at 850 °C dipoles and debris are completely absent (Appel et al., 2010). At this temperature dynamic recovery has probably fully taken place, which is consistent with the cycling softening observed at this temperature. It remains to determine, how these recovery mechanisms are manifested in the recovery of the flow stress of fatigued specimen.

4. Conclusions

The defect structure produced by monotonic and cyclic room temperature deformation of Ti-rich TiAl alloys was analyzed by mechanical testing and electron microscope observations.

A significant component of the substructure, common to both monotonic and cyclic hardening, is a dispersion of fine dislocation debris and probably a significant vacancy supersaturation.

The debris is produced by jog dragging ordinary screw dislocations, which give rise to a strain dependent stress increment and thus contributes strain hardening.

By virtue of their small defect volume, the excess vacancies and debris are prone to static and dynamic recovery.

A simulation study was performed that describes the annihilation of excess vacancies at dislocations and debris. The process is driven by the thermodynamic force resulting from the chemical potential of the excess vacancies. The model can account for the rapid kinetics of static recovery.

Acknowledgements

F.A. acknowledges the continuous support of St. Eggert, U. Lorenz, M. Oehring, and J. Paul, from the Helmholtz-Zentrum Geesthacht, Germany. Thanks are due to Th. Heckel, A. El-Chaikh and H.-J. Christ from Universität Siegen, Germany, for performing the fatigue experiments. The financial support by the Deutsche Forschungsgemeinschaft (Projects AP 49/5 and AP 49/4-6) is gratefully acknowledged.

F.D.F. expresses his thanks to Dr. E. Gamsjäger for performing the numerical work (fitting etc.).

F.D.F., E.K. and J.S. acknowledge gratefully the financial support by the Austrian Federal Government (in particular from the Bundesministerium für Verkehr, Innovation und Technologie and the Bundesministerium für Wirtschaft und Arbeit) and the Styrian Provincial Government, represented by Österreichische Forschungsförderungsgesellschaft mbH and by Steirische Wirtschaftsförderungsgesellschaft mbH, within the research activities of the K2 Competence Centre on "Integrated Research in Materials, Processing and Product Engineering", operated by the Materials Center Leoben Forschung GmbH in the framework of the Austrian COMET Competence Centre Programme as well as funding through DFG project AB.314/1 (FOR 741).

J.S. acknowledges gratefully the financial support by the Czech Science Foundation in the frame of project P108/10/1781 and by the Research Plan of the Institute of Physics of Materials (project CEZ:AV0Z20410507).

References

Appel, F., 1989. On the intersection of oblique screw dislocations. Phys. Status Solidi (a) 116, 153-163.

Appel, F., 1991. An electron-microscope study of the origin of latent hardening in NaCl. Philos. Mag. A 63, 71-85.

Appel, F., Wagner, R., 1995. Deformation mechanisms in TiAl/Ti_3Al structures. In: Kim, Y-W., Wagner, R., Yamaguchi, M. (Eds.), Gamma Titanium Aluminides. TMS, Warrendale, PA, pp. 231-244.

Appel, F., Lorenz, U., Oehring, M., Sparka, U., Wagner, R., 1997. Thermally activated deformation mechanisms in micro-alloyed titanium aluminide alloys. Mater. Sci. Eng. A 233, 1-14.

Appel, F., Wagner, R., 1998. Microstructure and deformation of two-phase gamma-titanium aluminides. Mater. Sci. Eng. R 22, 187-268.

Appel, F., Sparka, U., Wagner, R., 1999. Work hardening and recovery of gamma base titanium aluminides. Intermetallics 7, 325-334.

Appel, F., 2005. An electron microscope study of mechanical twinning and fracture in TiAl alloys. Philos. Mag. 85, 205-231.

Appel, F., Heckel, Th., Christ, H.-J., 2010. Electron microscope characterization of low cycle fatigue in a high-strength multiphase titanium aluminide alloy. Int. J. Fatigue 32, 792-798.

Bacon, D.C., Bullough, R., Willis, J.R., 1970. The anisotropic elastic energy of a rhombus-shaped dislocation loop. Philos. Mag. 22, 31-45.

Beyerlein, I.J., Tomé, C.N., 2008. A dislocation based constitutive law for pure Zr including temperature effects. Int. J. Plasticity 24, 867-895.

Brockman, R.A., 2003. Analysis of elastic-plastic deformation in TiAl polycrystals. Int. J. Plasticity 19, 1749-1772.

Bullough, R., Newman, R.C., 1970. Kinetics of migration of point defects to solids. Rep. Prog. Phys. 33, 101-148.

Chen, H.S., Gilman, J.J., Head, A.K., 1964. Equilibrium of extended dislocations within edge dislocation dipoles. Philos. Mag. 10, 35-42.

Chen, H.S., Head, A.K., Gilman, J.J., 1964. Dislocation multipoles and their role in strain hardening. J. Appl. Phys. 35, 2502-2514.

El-Chaikh, A., Heckel, Th., Christ, H.-J., 2011. Thermomechanical fatigue of titanium aluminides. Int. J. Fatigue (2011), doi: 10.1016/j.ijfatigue.2011.08.005.

Feng, Q., Whang, S.H., 2000. Deformation of Ti-56 at. %Al single crystal oriented for single slip by 1/2<110] ordinary dislocations. Acta Mater. 48, 4307-4321.

Fischer, F.D., Svoboda, J., Appel, F., Kozeschnik, E., 2011a. Modelling of excess vacancy annihilation at different types of sinks. Acta Mater. 59, 3463-3472.

Fischer, F.D., Svoboda, J., 2011b. Chemically and mechanically driven creep due to generation and annihilation of vacancies with non-ideal sources and sinks. Int. J. Plasticity, 27, 1384-1390.

Fröbel, U., Appel, F., 2002. Strain ageing in γ(TiAl)-based titanium aluminides due to antisite atoms. Acta Mater. 50, 3693-3707.

Gao, Y., Zhuang, Z., Liu, Z.L., You, X.C., Zhao, X.C., Zhang, Z.H., 2011. Investigations of pipe-diffusion-based dislocation climb by discrete dislocation dynamics. Int. J. Plasticity 27, 1055-1071.

Gilman, J.J., 1962. Debris mechanism of strain hardening. J. Appl. Phys. 33, 2703-2709.

Gray III, G.T., Pollock, T.M., 2002. Strain hardening. In: Westbrook, J.H., Fleischer, R.L., (Eds.), Intermetallic Compounds. Vol. 3, Principles and Practice. John Wiley & Sons, Ltd, Chichester, pp. 361-377.

Hansen, N., Jensen, D.J., 2011. Deformed metal - structure, recrystallization and strength. Mater. Sci. Technol. 27, 1229-1240.

Heckel, Th., Christ, H.-J., 2010. Isothermal and thermomechanical fatigue of titanium alloys. Proc. Eng. 2, 845-854.

Hemker, K.J., Viguier, B. Mills, M.J., 1993. Dislocation core structures in the ordered intermetallic alloy TiAl. Mater. Sci. Eng. A 164, 391-394.

Hénaff, G., Gloanec, A.-L., 2005. Fatigue properties of TiAl alloys. Intermetallics 13, 543-558.

Herrmann, D., Appel, F., 2009. Diffusion bonding of γ(TiAl) alloys: influence of composition, microstructure, and mechanical properties. Metall. Mater. Trans. A, 40A, 1881-1902.

Hirth, J.P., Lothe, J., 1992. Theory of Dislocations. Krieger, Melbourne.

Jiao, Z., Whang, S.H., Yoo, M.H., Feng, Q., 2002. Stability of ordinary dislocations on cross-slip planes in gamma-TiAl. Mater. Sci. Eng. A 329-331, 171-176.

Kocks, U.F., Argon, A.S., Ashby, M.F., 1975. Thermodynamics and kinetics of slip. Prog. Mater. Sci. 19, 1-281.

Kocks, U.F., Mecking, H., 2003. Physics and phenomenology of strain hardening: the FCC case. Prog. Mater. Sci. 48, 171-273.

Kroupa, F., 1962. Interaction between prismatic dislocation loops and straight dislocations. Philos. Mag. 7, 783-801.

Kroupa, F., 1966a. Force between a dislocation dipole and a non-parallel dislocation. Acta metall. 14, 60-61.

Kroupa, F., 1966b. Dislocation dipoles and dislocation loops. J. de Physique 27, C3-154-C3-167.

Li, Y.G., Loretto, M.H., 1995. Tensile properties and microstructure of Ti-48Al-2Nb and Ti48Al-8Nb. Phys. Status Solidi (a) 150, 271-280.

Marketz, W.T., Fischer, F.D., Clemens, H., 2003. Deformation Mechanisms in TiAl Intermetallics - Experiments and Modeling. Int. J. Plasticity 19, 281-321.

Mishin,Y., Herzig, Chr., 2000. Diffusion in the Ti-Al system. Acta Mater. 48, 589-623.

Schafrik, R.E., 1977. Dynamic elastic moduli of titanium aluminides. Metall. Trans. A, 8A, 1003-1006.

Schöck, G., 1965. Activation energy of dislocation movement. Phys. Status Solidi 8, 499-507.

Singh, J.B., Molénat, G., Sundararaman, M., Banerjee, S., Saada, G., Veyssière, P., Couret, A., 2006. In situ straining investigations of slip transfer across α_2 lamellae at room temperature in lamellar TiAl alloy. Philos. Mag. 86, 47-60.

Sriram, S., Dimiduk, D.M., Hazzledine, P.M., Vasudevan, V.K., 1997. The geometry and nature of pinning points of 1/2<001] unit dislocations in binary TiAl alloys. Philos. Mag. A 76, 965-993.

Sun, Y.Q., 1999. Anisotropic line tension of 1/2<110] screw dislocations on cross-slip in gamma TiAl. Philos. Mag. Lett. 79, 539-544.

Thomas, G. , Goringe M.A., 1979. Transmission Electron Microscopy of Materials. John Wiley, New York.

Thornton, P.H., Cahn, R.W., 1961. The high temperature electrical resistance of iron-aluminium alloys. Philos. Mag. 6, 1093-1101.

Vasudevan, V.K., Stucke, M.A., Court, S.A., Fraser, H.L., 1989. The influence of 2nd phase Ti_3Al on the deformation mechanisms in TiAl. Philos. Mag. Lett. 59, 299-307.

Veyssière, P., Douin, J., 1995. Dislocations. In: Westbrook, J.H., Fleischer, R.L., (Eds.), Intermetallic Compounds. Vol. 1, Principles. John Wiley & Sons, Ltd, Chichester, pp. 519-558.

Wang, B-Y., Wang, Y-X., Gu, Q., Wang, T-M., 1997. The threshold displacement and interstitial atom formation energy in TiAl alloy. Comput. Mater. Sci. 8, 267-272.

Wiezorek, J.K.M., Zhang, M.H., Fraser, H.L., 2000. Mechanisms of plasticity and fracture of partially lamellar titanium aluminium. Intermetallics 8, 99-113.

Yoo, M.H., Fu, C.L., 1998. Physical constants, deformation twinning, and microcracking of titanium aluminides. Metall. Mater. Trans. A, 29A, 49-63.

Zehetbauer, M., 1994. Effects on non-equilibrium vacancies on strengthening. Key Eng. Mater. 97-98, 287-306.

Table 1. Composition, microstructure and mechanical properties of the alloy investigated in recovery experiments; σ_{WH} (flow stress) and $1/V$ (reciprocal activation volume) determined after compression to strain ε_p=7.5 % at T=295 K and $\dot{\varepsilon} = 2.08\text{x}10^{-5}$ s^{-1}; D (grain size), D_C (colony size), λ (lamellar spacing).

Nr./ Symbol	Composition (at. %)	Microstructure	σ_{WH} (MPa)	$10^{-18}/V$ (mm^{-3})	Ref.
1	Ti-45Al-5Nb-0.2B-0.2C	nearly globular, D=1-8 μm	1350	1.03	[1]
2a	Ti-45Al-8Nb-0.2C	duplex, D=5-10 μm, D_C=10-30 μm	1330	1.08	[1]
2b	Ti-45Al-7.7Nb-0.2C	nearly lamellar with 66 % lamellar colonies, D=3.5 μm, D_C=5.9 μm	1600	1.07	[1]
3	Ti-45Al-10Nb	duplex	1427	1.09	[1]
4, ∗	Ti-48Al-2Cr	nearly lamellar, D_C=1mm, λ=0.05-1 μm	1029	0.53	[1]
5, ○	Ti-47Al-2Cr-0.2Si	equiaxed $\alpha_2+\gamma$, D=11 μm	947	0.7	[2]
6, ▽	Ti-47Al-2Cr-0.2Si	nearly lamellar, D_C=330 μm λ=0.05-1 μm	1065	1.12	[2]
7, ◇	Ti-52Al-2Cr	near γ, D=5.2 μm	1037	0.7	[2]
8, △	Ti-54Al	near γ, D=188 μm	901	0.75	[2]

[1] this paper; [2] Appel et al. (1999)

Table 2. Recovery of the flow stress after work hardening to strain ε_p=7.5% at the annealing temperatures 973 K and 1053 K; data determined on a forged Ti-47Al-2Cr-0.2 Si alloy with a globular ($\alpha_2+\gamma$) microstructure (Appel et al., 1999). Fitting of the data according Eq. (9.2) with the parameters $\tilde{a}$ and $\tilde{c} = 1/100C$.

t [min]	$\kappa = (\sigma_R - \sigma_0)/(\sigma_{WH} - \sigma_0)$	$\tilde{a}$	$\tilde{c}$
973 K			
0	1	2.9224	0.569
15	0.870		
45	0.812		
105	0.758		
225	0.715		
1053 K			
0	1	0.290	0.850
15	0.930		
45	0.853		
105	0.789		
225	0.726		